

## Investigation of the high spin structure of $^{88}\text{Zr}$

S. Saha,<sup>1</sup> R. Palit,<sup>1,\*</sup> J. Sethi,<sup>1</sup> S. Biswas,<sup>1</sup> P. Singh,<sup>1</sup> T. Trivedi,<sup>1</sup> D. Choudhury,<sup>1</sup> and P. C. Srivastava<sup>2</sup>

<sup>1</sup>*Department of Nuclear and Atomic Physics, Tata Institute of Fundamental Research, Mumbai - 400005, India*

<sup>2</sup>*Department of Physics, Indian Institute of Technology, Roorkee - 247667, India*

(Received 14 February 2014; revised manuscript received 24 March 2014; published 16 April 2014)

High spin states of  $^{88}\text{Zr}$  were populated with  $^{80}\text{Se}(^{13}\text{C}, 5n)$  fusion evaporation reaction. A thin target as well as Au backed target were used in two different experiments for the present study. Excited levels of  $^{88}\text{Zr}$  have been observed up to spin  $\sim 20\hbar$  and an excitation energy of  $\sim 10$  MeV. Spin and parity of most of the states have been determined from directional correlation and polarization measurements. The level scheme was substantially extended with the addition of a number of high spin states and transitions. The comparison of the measured levels of  $^{88}\text{Zr}$  with large shell model calculations based on the full unrestricted  $f_{5/2}p_{g_{9/2}}$  model space established the dominance of shell-model excitation up to the highest observed spin.

DOI: [10.1103/PhysRevC.89.044315](https://doi.org/10.1103/PhysRevC.89.044315)

PACS number(s): 21.10.Hw, 25.70.Gh, 27.50.+e, 29.30.Kv

### I. INTRODUCTION

High spin spectroscopy of nuclei near shell closure remains a subject of current interest in nuclear physics. Due to the limited available valence space for particle excitation, shell model calculation is very useful to interpret the experimental spectrum in this region. Measurements with modern large  $\gamma$  ray detector arrays have made it possible to identify excitations up to high spin in these nuclei [1–4]. A theoretical interpretation of these high spin excited states requires shell model calculations involving larger model space which are currently being developed. In particular, an optimum shell model interaction in the  $f_{5/2}p_{g_{9/2}}$  model space is being prescribed to explain the excitation in nuclei close to  $^{100}\text{Sn}$  and  $^{56}\text{Ni}$ . According to a recent review, no shell model interaction is yet optimized in this model space [5]. The experimental data at high spin will give a stringent test to the available shell model interaction in this region. Nuclei around  $^{90}\text{Zr}$  having  $Z = 40$  subshell closure and  $N = 50$  shell closure are good candidates to compare such interactions. In our recent work, a detailed comparison of the measured excited levels of  $^{89}\text{Zr}$  [6] up to high spin with the results from the shell model calculations based on the JUN45 [5] and jj44b [7] interactions has been carried out. Excellent agreement of the calculation to the experimental level scheme of  $^{89}\text{Zr}$  has been observed. However, similar experimental verifications up to high spin states in the nearby isotopes are needed to test the universality of these interactions in the  $f_{5/2}p_{g_{9/2}}$  model space. With this motivation, here we will present our study of high spin states in the  $^{88}\text{Zr}$  nucleus and compare our result with the same two interactions.

The earlier spectroscopic studies of  $^{88}\text{Zr}$  were carried out via  $\beta$  decay of  $^{88}\text{Nb}$  [8–11], two-neutron transfer reaction  $^{90}\text{Zr}(p,t)$  [12,13], and light charged particle induced fusion evaporation reactions  $^{86}\text{Sr}(\alpha,2n\gamma)$  [14,15],  $^{89}\text{Y}(\alpha,p4n\gamma)$  [16], and  $^{89}\text{Y}(p,2n\gamma)$  [15] reactions. Till date, the highest spin of  $^{88}\text{Zr}$  was reported by Warburton *et al.* [17] using  $^{74}\text{Ge}(^{18}\text{O},4n\gamma)$  reaction with smaller arrays consisting of a

few NaI detectors, 2–3 coaxial germanium detectors, and LEPS. In the present work, the previously established level scheme of  $^{88}\text{Zr}$  has been modified with around 25 newly assigned transitions. The details of the analysis procedure and experimental results are discussed in this paper. The level scheme of  $^{88}\text{Zr}$  developed in the current work is compared with the predictions of the large scale shell model calculations based on two recently developed residual interactions.

### II. EXPERIMENTAL DETAILS AND ANALYSIS

Excited states of  $^{88}\text{Zr}$  were produced by bombarding a  $^{13}\text{C}$  beam from TIFR-BARC Pelletron Linac Facility (PLF) at 60 MeV on a  $500 \mu\text{g}/\text{cm}^2$   $^{80}\text{Se}$  target evaporated on an aluminum foil of  $80 \mu\text{g}/\text{cm}^2$  thickness. The target was mounted on a tantalum frame with the aluminum backing facing the incident beam. The  $\gamma$  rays emitted in the reaction have been measured with the Indian National Gamma Array (INGA) at TIFR which is a Compton suppressed clover detector array with a provision of placing 24 clovers at various angles with respect to the beam direction. The available angles in the array are  $23^\circ$ ,  $40^\circ$ ,  $65^\circ$ ,  $90^\circ$ ,  $115^\circ$ ,  $140^\circ$ , and  $157^\circ$ . While six detectors can be kept at  $90^\circ$  with respect to the beam direction [18], the rest of the angles can accommodate three detectors each. In the present experiment, four clover detectors were kept at  $90^\circ$ , three detectors each at  $40^\circ$ ,  $115^\circ$ ,  $140^\circ$ ,  $157^\circ$ , and two detectors at  $65^\circ$ . Two- and higher-fold clover coincidence events were recorded in a fast digital data acquisition system based on Pixie-16 modules of XIA LLC [19,20]. For angular distribution and photopeak efficiency measurements, the digital data acquisition system has been used in singles mode.

The target was sufficiently thin so that the residual nucleus can fly through it. The  $\gamma$  rays from the recoiling residual nucleus escaping the thin target were corrected for Doppler shifts at different angles according to the formula

$$E_\gamma = E_0(1 + \beta \cos \theta), \quad (1)$$

where  $E_\gamma$  is the energy of the Doppler shifted  $\gamma$  ray emitted from a recoiling nuclei moving with a velocity  $v$  observed in a detector kept at an angle  $\theta$  with respect to the beam direction.

\*Corresponding author: palit@tifr.res.in

$E_0$  is the energy of the  $\gamma$  ray in co-moving frame and  $\beta = \frac{v}{c}$ . The data sorting routine ‘‘Multi pARAmeter time-stamped based COincidence Search program (MARCOS)’’ developed at TIFR was used for gain matching, Doppler shift correction, and to generate the  $E_\gamma - E_\gamma$  matrix and  $E_\gamma - E_\gamma - E_\gamma$  cube which were later converted to RADWARE format and the analysis was done using the RADWARE package [21].

The change in spin of a nucleus can be determined by measuring the multipolarity of the emitted  $\gamma$  ray. In the case of a stretched cascade of  $\gamma$  rays the multipolarity of transitions can uniquely determine the spin of a given nuclear state. Multipolarity of a given transition can be obtained from the angular distribution and directional correlation of oriented states (DCO) method [22,23]. Angular distribution of a few transitions with energies 101, 399, and 1022 keV have been obtained to reconfirm their multipolarities reported in Ref. [17]. The angular distribution measurements suggest  $\Delta J = 1$  for 101 and 399 keV transitions and  $\Delta J = 2$  for 1022 keV transition (see the footnote of Table I for the angular distribution coefficients obtained in the present measurement). Mainly, these transitions have been used for gating purpose to extract the DCO ratios. In the present INGA geometry the DCO ratios ( $R_{\text{DCO}}$ ) are obtained from the intensity ratio of the coincident events detected at angles  $157^\circ$  and  $90^\circ$  with respect to the beam direction, respectively. The  $R_{\text{DCO}}$  is obtained from the formula

$$R_{\text{DCO}} = \frac{I(\gamma_1) \text{ at } 157^\circ \text{ gated by } \gamma_2 \text{ at } 90^\circ}{I(\gamma_1) \text{ at } 90^\circ \text{ gated by } \gamma_2 \text{ at } 157^\circ},$$

where  $I(\gamma_1)$  represents the intensity of  $\gamma_1$  measured in coincidence with  $\gamma_2$ . The DCO ratio values of stretched dipole and quadrupole transitions are  $\sim 0.5(1.0)$  and  $\sim 1.0(2.0)$ , respectively, for a pure quadrupole (dipole) gate.

In the present INGA geometry, the  $90^\circ$  clover detectors have their crystals arranged parallel and perpendicular to the reaction plane. This geometry facilitates the use of clover detectors as Compton polarimeters [24,25]. The electric or magnetic nature of the  $\gamma$  rays are identified from the asymmetry of the scattered  $\gamma$  ray to parallel and perpendicular directions with respect to the reaction plane [26,27]. For a Compton-polarimeter, polarization asymmetry of a transition,  $\Delta$ , is defined as [26]

$$\Delta = \frac{a(E_\gamma)N_\perp - N_\parallel}{a(E_\gamma)N_\perp + N_\parallel}, \quad (2)$$

where  $N_\parallel(N_\perp)$  is the number of  $\gamma$  transitions scattered parallel (perpendicular) to the reaction plane and  $a(E_\gamma)$  is a correction factor for the parallel to perpendicular scattering asymmetry within the crystals of a clover. For clover detectors used at  $90^\circ$  with respect to the beam direction  $a(E_\gamma)$  was found to be 1.00(1) from the  $^{133}\text{Ba}$  and  $^{152}\text{Eu}$  radioactive decay measurement. For a linear polarization measurement, two asymmetric matrices were constructed with events corresponding to parallel or perpendicular scattered  $\gamma$  rays at  $90^\circ$  detectors in coincidence with a  $\gamma$  ray detected at any other angle. This analysis scheme to extract the polarization asymmetry is referred as the integrated polarization direction correlation method [26]. In the case of unmixed stretched transition,

a positive (negative) value of the polarization asymmetry indicates its electric (magnetic) nature [28].

Presence of a long-lived isomer with  $T_{1/2} = 1.7\mu\text{s}$  at excitation energy  $E_x = 2888$  keV and spin  $J^\pi = 8^+$  restricts the coincidence of lower  $\gamma$  cascades with transitions above the isomer in the thin target experiment. Hence, this measurement using a thin target was complemented by the prompt-delayed analysis of data available using the reaction  $^{13}\text{C}(^{80}\text{Se},5n)$  at a 50 MeV beam energy with a Au backed  $^{80}\text{Se}$  target carried out in the same setup.

The backing material has been chosen to be of sufficient thickness to stop the recoil within the backing material and carry out the prompt-delayed coincidence analysis to look for the coincidence of transitions across the isomer in  $^{88}\text{Zr}$ . The prompt  $\gamma$  rays in coincidence (within a time window of 100 ns) with a 1022 keV transition are shown in Fig. 1 and they are emitted from various levels above the isomer. The transitions below the isomer are absent in this prompt spectrum. The inset displays the  $\gamma$  rays emitted following the 1022 keV transition by 1.0–1.5  $\mu\text{s}$ . Previously known transitions depopulating from the 2888 keV isomeric levels, namely, 77, 272, 671, 399, 1083, and 1057 keV lines [17] have been observed in our delayed spectrum. The observation of the decay below the isomer by gating on the 1022 keV transition above confirms the connection between the prompt and delayed  $\gamma$  rays reported in the previous work [17]. Some of the new transitions with energy 409 and 457 keV present in the prompt spectrum are marked with the asterisks and placed in the level scheme.

Most of the new assignments of  $\gamma$  rays in  $^{88}\text{Zr}$  have been based on the analysis of the threefold coincidence data from the thin target experiment. Using a double gate on previously known transitions above the isomer about 25 new transitions have been assigned to the level scheme of  $^{88}\text{Zr}$  (see Fig. 2). To identify weaker transitions the sum of double gates has been used to enhance statistics. The new transitions are indicated by red and the rearranged transitions are indicated by green in Fig. 2. Intensities of all the transitions above the isomer have been normalized with respect to that of the 1022 keV transition. The relative intensity of a transition in the level scheme is roughly proportional to the thickness of the arrow describing the corresponding  $\gamma$  ray.

### III. RESULTS

In the  $^{88}\text{Zr}$  nucleus, because of the dominance of single particle excitations, band-like structure is not expected up to the medium spin range. However, to simplify the spectroscopic description of the complicated high spin level structure, it has been arranged in a different sequence of levels such that levels with the same spin and parity do not lie in the same sequence. As shown in the present level scheme (see Fig. 2), the positive parity states have been grouped as P1 to P3 along with the cascade G comprised of  $\gamma$  rays with energies 503, 1022, 816, and 1009 keV. A group of levels identified as P4 decay mainly to different states of P1 and P2. Unlike the multiple sequences of the positive parity states, the majority of the negative parity states are connected like one long chain of  $\gamma$  rays. The result of the  $\gamma$ - $\gamma$ - $\gamma$  analysis will be described in detail in this section. The energy, spin, and parity of different levels along with

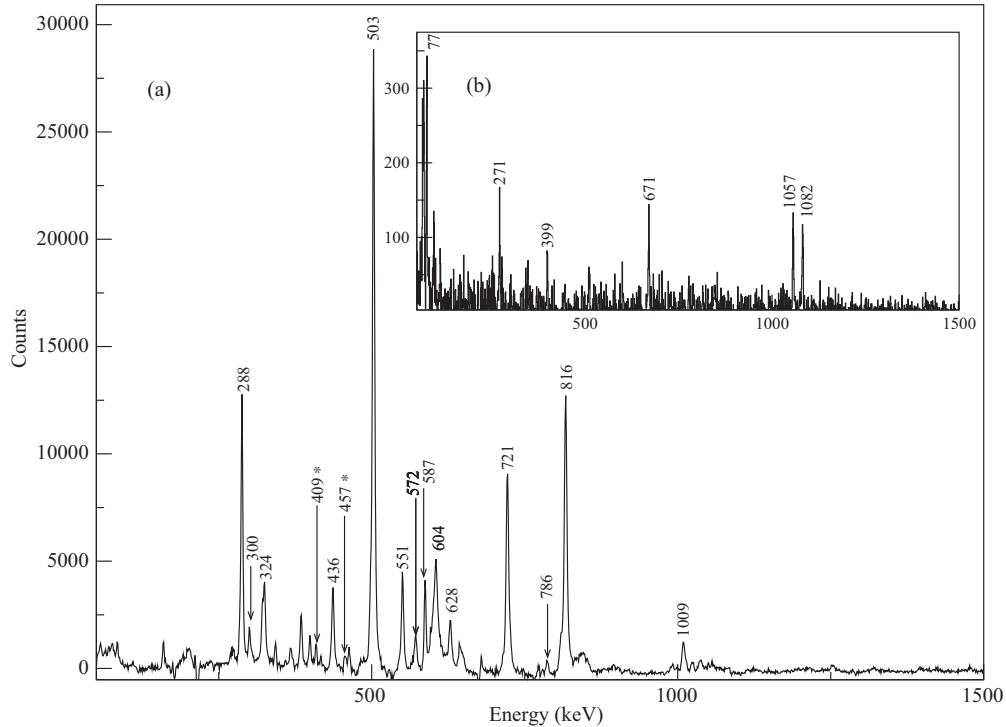


FIG. 1. Prompt and delayed coincidence spectrum of  $^{88}\text{Zr}$  with a gate on the 1022 keV transition are shown in (a) and (b), respectively. Due to the presence of a  $T_{1/2} = 1.7 \mu\text{s}$  isomeric level at 2888 keV, energy in the prompt coincidence (within a time window of 100 ns) spectrum none of the transitions below this level are observed. However, the strong transitions below the isomer could be exclusively identified from the delayed coincidence spectrum as shown in the inset. The  $\gamma$  rays that have been newly observed in the present experiment are marked with asterisks.

the intensity, DCO ratio, and polarization asymmetry of the observed  $\gamma$ -ray transitions are mentioned in Table I.

### A. Positive parity states

As mentioned earlier the  $\gamma$  rays depopulating the  $8^+_{17}$  isomeric state could be observed in delayed coincidence with respect to the 1022 keV transition, present above the isomeric state. The 1009, 816, 1022, and 503 keV  $\gamma$  rays are found to be in coincidence in the Au-backed target experiment and are placed according to their intensity in the main cascade G. The placement of these  $\gamma$  rays in the present work are found to be consistent with the previous literature. The two strong transitions in the cascade G with energies 503 and 1022 keV have been assigned as  $\Delta J = 0$  and  $\Delta J = 2$ , respectively, in Ref. [17]. As mentioned before, the  $\Delta J = 2$  nature of the 1022 keV transition has also been reconfirmed with angular distribution measurement in the present experiment. Multipolarities of most of the transitions in the positive parity part of the level scheme are determined from the DCO ratios extracted with 1022 keV gate.

The group of positive parity states marked as P1 has a cascade of  $\gamma$  rays with energies of 285, 551, 325, 605, 597, and 678 keV. The lowest energy state in this group has the excitation energy of 5666 keV and a spin of  $J^\pi = 12^+$ . With the measured multipolarities of the various  $\gamma$  rays, the P1 sequence has been extended up to spin  $J^\pi = 18^+$  having an excitation energy of 8706 keV. The 6826 keV level has also

a parallel decay out to the ground sequence at the 6239 keV level through a 587 keV transition. Again, the  $13^+$  5951 keV level of the sequence has a 288 keV feeding from the  $14^+$  6239 keV level. The parallel branch can be observed from Fig. 3, which is a sum of the double gates of 503, 1022, 816, and 721 keV  $\gamma$  ray with a 587 keV  $\gamma$  ray. The 288 keV  $\gamma$  ray is strongly observed in this spectrum while the 325 keV  $\gamma$  ray is found to be absent. Whereas, Fig. 4, which is a sum of double gated coincident spectrum with 503, 1022, 816, and 721 keV  $\gamma$  rays with 551 keV  $\gamma$  ray, shows the presence of 325 keV line and the absence of 288 and 587 keV lines. The above observation confirms the assignment of the  $\gamma$  rays in the level scheme. The ordering of the 551 and 325 keV  $\gamma$  rays were done according to their intensity. The 721 keV  $\gamma$  ray has been assigned as a stretched  $M1$  transition from the observed DCO ratio of 0.43(4) in the 1022 keV gate and polarization asymmetry of  $-0.10(2)$ . Hence, the spin of the 5951 keV level is assigned as  $13^+$ . The DCO ratios of 551, 325, and 604 keV  $\gamma$  rays are  $\sim 0.5$  with a quadrupole gate and the same for the 597 keV transition is  $\sim 1$  with a dipole gate. The measured polarization asymmetry of all the above-mentioned transitions are negative. The cascade of  $\gamma$  rays 551, 325, 604, and 597 keV are therefore assigned as a stretched  $M1$  character.

In the positive parity part of the reported level scheme of  $^{88}\text{Zr}$  [17], the placement of a 628 keV  $\gamma$  ray decaying from the 6578 keV to 5951 keV level [17] has been changed in the present work. The 628 keV  $\gamma$  ray has now been reassigned as decaying from the 7615 keV to 6987 keV level. This new

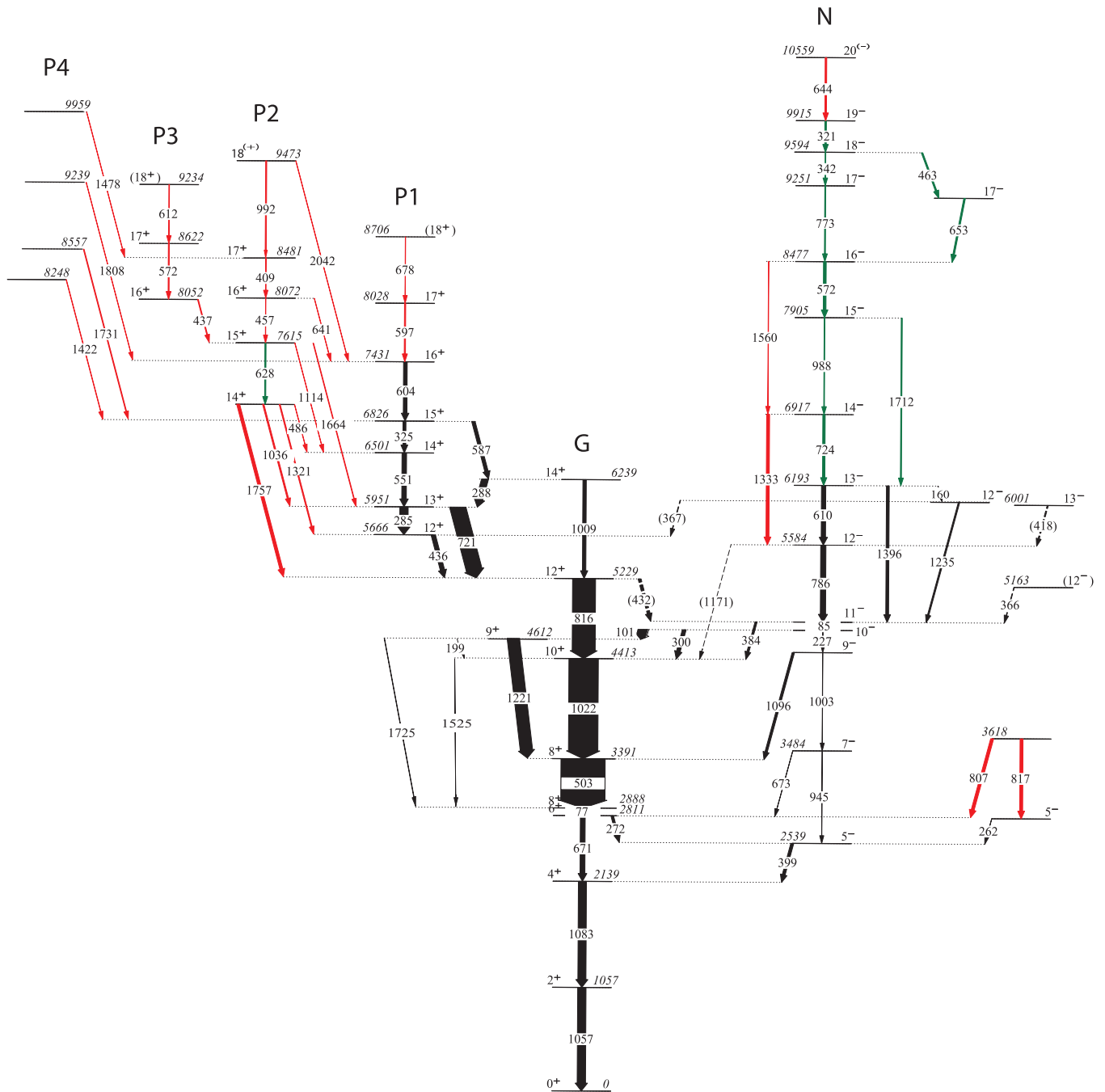
$^{88}\text{Zr}$  Level Scheme

FIG. 2. (Color online) Partial level scheme of  $^{88}\text{Zr}$  developed in the present work. The energies of the observed excited states and  $\gamma$ -ray transitions are given in keV. The thickness of the arrows above the 2888 keV level are roughly proportional to the  $\gamma$ -ray intensity mentioned in Table I. The new and rearranged  $\gamma$  rays are marked with red and green color, respectively.

assignment was based on 1757, 1036, 1321, and 486 keV transitions observed in coincidence with 628 keV in different combination of double gates. The 1036, 1321, and 1757 keV  $\gamma$  rays are shown in Fig. 5. Above the 7615 keV level a cascade of three new transitions of 457, 409, and 992 keV are placed in group P2. The 457 and 409 keV transitions are shown in Fig. 4, while the 992 keV transition is depicted in Fig. 5. A 2042 keV transition has also been decaying from the observed topmost

level of the cascade viz. the 9473 keV to 7431 keV level. The DCO ratio of the 1757 keV transition decaying from the 6987 keV level to the 5229 keV level of  $J^\pi = 12^+$  is found to be 1.17(12) in the 1022 keV gate. The quadrupole nature of the transition makes the band head spin of the cascade  $J^\pi = 14^{(+)}$ . The DCO ratios of the 628, 409, and 457 keV transitions with the same gate are found to be around 0.5, which indicate their  $M1$  character. The topmost transition 992 keV is also assigned

TABLE I. Excitation energies of levels ( $E_i$ ) in keV,  $\gamma$ -ray energies ( $E_\gamma$ ) in keV, intensities,  $R_{\text{DCO}}$ , polarization asymmetry ( $\Delta$ ) value, and initial and final state spins of the transitions of  $^{88}\text{Zr}$  deduced from the present work are listed. The uncertainties in the energies of  $\gamma$  rays are 0.3 keV for intense peaks and 0.7 keV for weak peaks.

$E_i$	$J_i^\pi \rightarrow J_f^\pi$	$E_\gamma$	$I_\gamma$	$R_{\text{DCO}}$	Gate <sub>DCO</sub>	$\Delta$
1057	$2^+ \rightarrow 0^+$	1056.9	–	–	–	–
2139	$4^+ \rightarrow 2^+$	1082.5	–	–	–	–
2811	$6^+ \rightarrow 5^-$	271.8	–	–	–	–
2811	$6^+ \rightarrow 4^+$	671.2	–	–	–	–
2888	$8^+ \rightarrow 6^+$	76.9	–	–	–	–
3391	$8^+ \rightarrow 8^+$	502.9	148(14) <sup>a</sup>	0.96(9)	1022	0.10(3)
4413	$10^+ \rightarrow 8^+$	1022.4 <sup>b</sup>	100	0.91(9)	816	0.11(1)
4413	$10^+ \rightarrow 8^+$	1525.1	0.22(3)	–	–	–
4612	$9^+ \rightarrow 10^+$	199.2	0.11(4)	–	–	–
4612	$9^+ \rightarrow 8^+$	1221.6	42(3)	0.54(5)	101	0.03(1)
4612	$9^+ \rightarrow 8^+$	1724.5	0.24(5)	–	–	–
5229	$12^+ \rightarrow 11^-$	431.9	–	–	–	–
5229	$12^+ \rightarrow 10^+$	816.4	78(6)	0.90(9)	1022	0.05(2)
6239	$14^+ \rightarrow 13^+$	288.1	23(2)	1.10(1)	721	-0.17(1)
6239	$14^+ \rightarrow 12^+$	1009.3	12(1)	1.0(1)	1022	0.06(2)
2801	$5^- \rightarrow 5^-$	261.7	–	–	–	–
3618	$\rightarrow 6^+$	806.9	–	0.75(7)	399	–
3618	$\rightarrow 5^-$	817.0	–	–	–	–
2539	$5^- \rightarrow 4^+$	399.4 <sup>c</sup>	–	–	–	0.01(2)
3484	$7^- \rightarrow 6^+$	672.8	–	–	–	–
3484	$7^- \rightarrow 5^-$	944.6	–	–	–	–
4486	$9^- \rightarrow 7^-$	1002.7	–	–	–	0.05(8)
4486	$9^- \rightarrow 8^+$	1095.6	8.6(6)	0.93(5)	786	0.05(2)
4713	$10^- \rightarrow 9^+$	100.8 <sup>d</sup>	32(2)	0.92(2)	786	–
4713	$10^- \rightarrow 9^-$	226.8	1.21(16)	0.84(3)	786	-0.26(13)
4713	$10^- \rightarrow 10^+$	299.9	12.6(6)	1.1(1)	1022	-0.30(2)
4798	$11^- \rightarrow 10^-$	84.5	22(1)	2.0(2)	101	–
4798	$11^- \rightarrow 10^+$	384.5	6.89(36)	0.54(5)	1022	0.19(12)
5584	$12^- \rightarrow 11^-$	786.2	18(1)	1.05(10)	101	-0.02(3)
5584	$12^- \rightarrow 10^+$	1170.8	<0.1	–	–	–
6193	$13^- \rightarrow 12^-$	160.4	1.32(9)	0.81(9)	101	–
6193	$13^- \rightarrow 12^-$	609.8	15(1)	0.92(10)	101	-0.06(4)
6193	$13^- \rightarrow 11^-$	1396.0	9.5(6)	2.30(24)	101	0.12(2)
6917	$14^- \rightarrow 13^-$	724.0	8.0(6)	0.85(8)	101	-0.05(1)
6917	$14^- \rightarrow 12^-$	1333.1	10(1)	1.93(13)	101	0.07(2)
7905	$15^- \rightarrow 14^-$	988.0	2.29(22)	0.89(9)	101	-0.01(2)
7905	$15^- \rightarrow 13^-$	1712.0	3.46(30)	–	–	–
8477	$16^- \rightarrow 15^-$	572.1	9.13(65)	1.11(12)	101	-0.06(2)
8477	$16^- \rightarrow 14^-$	1560.1	1.25(11)	2.19(18)	101	–
9251	$17^- \rightarrow 16^-$	772.8	3.22(25)	0.66(7)	101	-0.02(1)
9594	$18^- \rightarrow 17^-$	342.5	2.18(12)	1.35(14)	101	-0.25(8)
9594	$18^- \rightarrow 17^-$	463.4	4.63(29)	1.20(12)	101	-0.15(8)
9915	$19^- \rightarrow 18^-$	321.4	5.3(3)	1.09(11)	101	-0.24(6)
10559	$20^{(-)} \rightarrow 19^-$	644.0	5.30(42)	1.23(12)	101	–
6032	$12^- \rightarrow 12^+$	366.6	1.86(96)	1.48(16)	101	–
6032	$12^- \rightarrow 11^-$	1234.9	4.78(34)	0.99(9)	101	-0.25(11)
9130	$17^- \rightarrow 16^-$	653.2	5.2(4)	0.89(2)	101	–
5163	$(12^-) \rightarrow 11^-$	365.6	1.86(13)	–	–	–
6001	$13^- \rightarrow 12^-$	417.7	3.86(21)	0.86(9)	101	-0.21(9)
5666	$12^+ \rightarrow 12^+$	436.5	14.7(9)	0.54(5)	1022	-0.09(6)
5951	$13^+ \rightarrow 12^+$	284.9	2.8(5)	0.94(4)	551	-0.06(5)
5951	$13^+ \rightarrow 12^+$	721.2	54(4)	0.43(4)	1022	-0.10(2)
6501	$14^+ \rightarrow 13^+$	550.6	15.6(9)	0.51(5)	1022	-0.14(7)

TABLE I. (Continued.)

$E_i$	$J_i^\pi \rightarrow J_f^\pi$	$E_\gamma$	$I_\gamma$	$R_{\text{DCO}}$	Gate <sub>DCO</sub>	$\Delta$
6826	$15^+ \rightarrow 14^+$	324.6	9.9(9)	0.50(5)	1022	-0.18(2)
6826	$15^+ \rightarrow 14^+$	587.2	11.4(9)	0.50(5)	1022	-0.08(1)
7431	$16^+ \rightarrow 15^+$	604.4	12.5(9)	0.64(6)	1022	-0.07(5)
8028	$17^+ \rightarrow 16^+$	597.0	4.0(8)	0.99(9)	721	-0.15(5)
8706	$(18^+) \rightarrow 17^+$	678.0	1.0(7)	–	–	–
6987	$14^+ \rightarrow 14^+$	485.6	1.0(6)	–	–	–
6987	$14^+ \rightarrow 13^+$	1036.1	4.4(4)	0.50(3)	1022	-0.15(3)
6987	$14^+ \rightarrow 12^+$	1321.0	3.35(26)	1.10(8)	816	–
6987	$14^+ \rightarrow 12^+$	1757.5	10.0(8)	1.17(12)	1022	–
7615	$15^+ \rightarrow 14^+$	628.0	3.8(3)	0.60(6)	1022	-0.03(7)
7615	$15^+ \rightarrow 14^+$	1113.6	1.0(7)	–	–	–
7615	$15^+ \rightarrow 13^+$	1664.1	1.95(24)	2.61(18)	721	–
8072	$16^+ \rightarrow 15^+$	457.0	1.05(15)	0.65(7)	1022	-0.02(2)
8072	$16^+ \rightarrow 16^+$	641.0	0.8(1)	–	–	–
8481	$17^+ \rightarrow 16^+$	409.0	1.95(7)	0.46(5)	1022	-0.08(3)
9473	$18^{(+)} \rightarrow 17^+$	992.0	6.9(5)	0.31(4)	1022	–
9473	$18^{(+)} \rightarrow 16^+$	2042.0	<0.1	–	–	–
8052	$16^+ \rightarrow 15^+$	437.0	2.7(3)	0.95(4)	721	-0.09(6)
8622	$17^+ \rightarrow 16^+$	571.9	3.23(19)	0.58(6)	1022	-0.06(2)
9234	$(18^+) \rightarrow 17^+$	612.1	<0.1	–	–	–
8248	$\rightarrow 15^+$	1422.0	1.30(18)	–	–	–
8557	$\rightarrow 15^+$	1731.3	2.49(10)	–	–	–
9239	$\rightarrow 16^+$	1808.0	1.05(20)	–	–	–
9959	$\rightarrow 17^+$	1478.0	<0.1	–	–	–

<sup>a</sup>Intensity of the 503 keV transition has been extracted from a 1083 keV gated prompt spectrum and has been normalized with the intensity of the 1022 keV transition.

<sup>b</sup>Angular distribution coefficients  $a_2 = 0.30(5)$  and  $a_4 = -0.11(5)$  for the 1022 keV transition suggests its  $\Delta J = 2$  nature.

<sup>c</sup>Angular distribution coefficients  $a_2 = -0.20(5)$  and  $a_4 = 0.04(4)$  for the 399 keV transition suggests its  $\Delta J = 1$  nature.

<sup>d</sup>Angular distribution coefficients  $a_2 = -0.29(5)$  and  $a_4 = 0.05(5)$  for the 101 keV transition suggests its  $\Delta J = 1$  nature.

as an  $M1$  transition with higher mixing due to its DCO ratio 0.31(4) with the same quadrupole gate.

A very weak cascade (P3) consisting of 437, 572 and 612 keV transition were seen in coincidence with 628 keV  $\gamma$ -rays. The 437 and 572 keV  $\gamma$ -rays are shown in the Fig. 4.

Four discrete  $\gamma$  rays of 1478, 1808, 1731, and 1422 keV energies have been observed to be feeding the P1 and P2 cascades at different levels. The 1478 and 1808 keV transitions have been assigned to be decaying to 8481 and 7431 keV levels, respectively. Whereas, the 1731 and 1422 keV  $\gamma$  rays are found to be populating the same 6826 keV level. The 1478 keV transition is shown in Fig. 5, while the 1422, 1731, and 1808 keV transitions are shown in Fig. 3. Due to low statistics of these high energy transitions, the spin and parity of these states could not be determined.

## B. Negative parity states

In the negative parity side of the previously known level scheme [17], several rearrangements of the levels have been proposed. Our new placement of levels is based on the observation of new crossover transitions for 1333 and

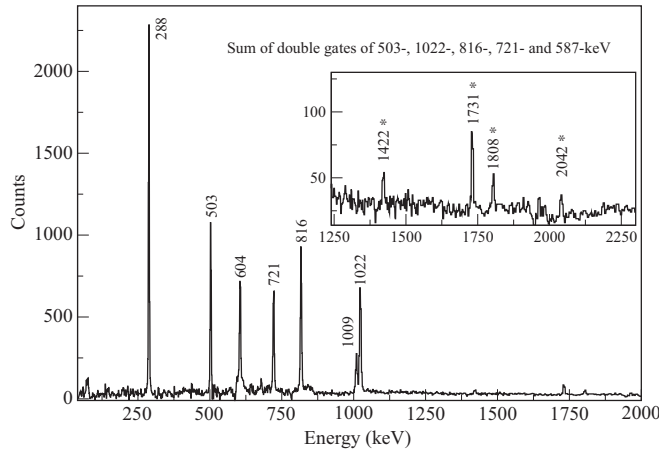


FIG. 3. Spectrum generated by the sum of the double gates of 503-587, 1022-587, 816-587, and 721-587 keV transitions. The strong transitions having energies of 288 and 604 keV belong to the cascade P1. The 2042 keV  $\gamma$ -ray links the cascades P2 and P1 at the 7431 keV level. The 1422, 1731, and 1808 keV  $\gamma$  rays belong to the sequence of levels marked as P4. The  $\gamma$  rays that have been newly observed in the present experiment are marked with asterisks.

1560 keV energies as shown in Fig. 6. This has also been supported with the measured intensities of various  $\gamma$  rays in our present work. The state with an excitation energy of 2539 keV and spin  $J^\pi = 5^-$  is the lowest energy negative parity state observed in our measurement. The negative parity states have been studied up to excitation energy of 10559 keV and spin  $J^\pi = 20^-$ . Our placement of  $\gamma$  rays with energies 945, 1003, 227, 85, 786, and 610 keV in the negative parity side up to excitation energy of 6193 keV and spin  $J^\pi = 13^-$  are in agreement with the previous level scheme reported in Ref. [17]. In fact, Warburton *et al.*, mentioned the uncertainty of the positions of the levels above 6193 keV (see caption of Fig. 3 of Ref. [17]). In their marginally most

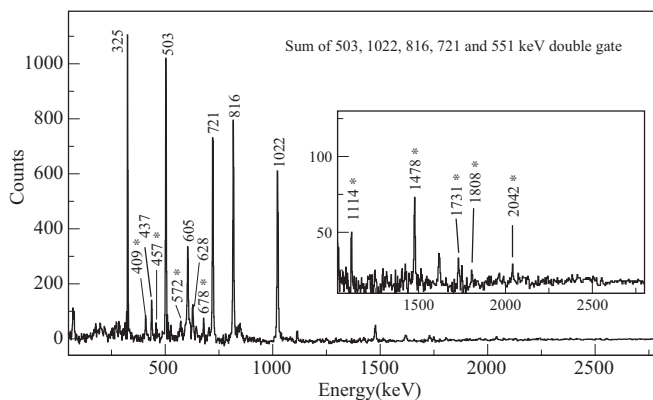


FIG. 4. Spectrum generated by the sum of the double gates of 503-551, 1022-551, 816-551, and 721-551 keV transitions. The strong transitions having energies of 325, 605, and 678 keV belong to cascade P1, while 409, 457, and 628 keV transitions belong to cascade P2 and the 437 and 572 keV transition belongs to the cascade P3 of positive parity part of the level scheme. The  $\gamma$  rays that have been newly observed in the present experiment are marked with asterisks.

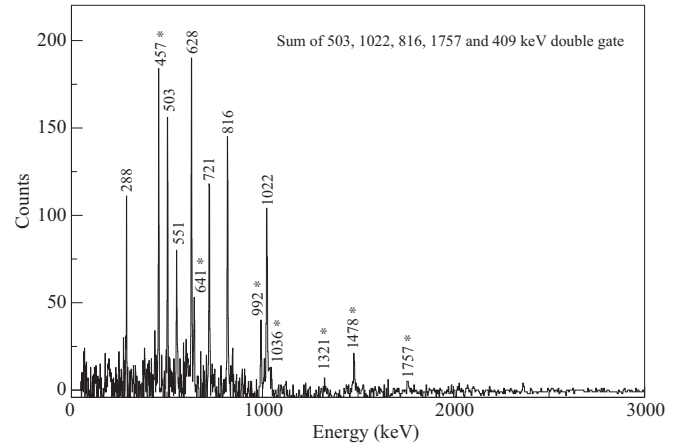


FIG. 5. Spectrum generated by the sum of the double gates of 503-409, 1022-409, 816-409, and 1757-409 keV transitions. The strong transitions having energies of 628, 457, and 992 keV belong to P2 while the 285 and 551 keV transitions belong to P1 of the positive parity part of the level scheme. The  $\gamma$  rays that have been newly observed in the present experiment are marked with asterisks.

probable arrangement, a 572 keV transition was feeding the 6193 keV level with spin  $J^\pi = 13^-$ . In the present experiment, parallel to the 610-724 keV sequence a crossover transition of energy 1333 keV has been observed (see Fig. 6). Similarly, another crossover transition with energy of 1560 keV has been observed to decay from the  $J^\pi = 16^-$  to  $J^\pi = 14^-$  level. Based on these crossover  $E2$ 's and level intensities the main cascade of  $\gamma$  rays has been rearranged with increasing level energy above the 6193 keV level as 724, 988, 572, 773, 342, 321, and 644 keV, respectively. The DCO ratio of most of the  $\gamma$  rays in the negative parity levels has been measured by putting a gate on the 101 keV transition decaying from the 4713 keV level. This transition was assigned as a  $\Delta J = 1, E1$  transition from the measured transition strength by Warbaton *et al.* as

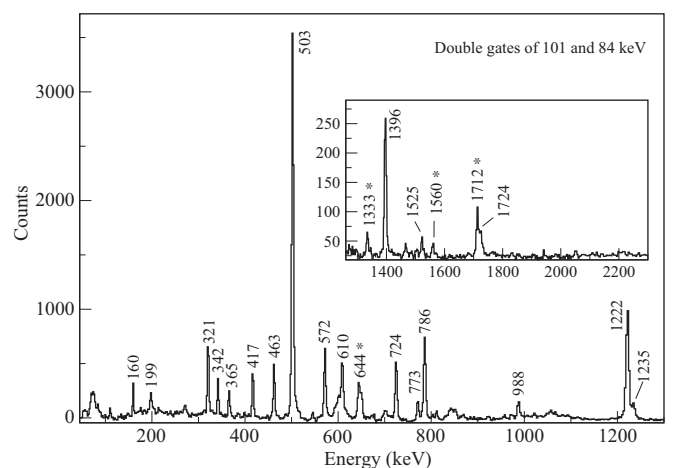


FIG. 6. Spectrum generated by the double gate of 101 and 84 keV transitions showing various  $\gamma$  rays associated with the decay of the negative parity states. The  $\gamma$  rays that have been newly observed in the present experiment are marked with asterisks.

$0.10 \times 10^{-3}$  Weisskopf units (W.u.) which is close to the recommended upper limit for  $E1$  transition that is  $10^{-2}$  W.u. [17]. The assigned  $\Delta J = 1$  nature of the 101 keV transition has also been reproduced in our angular distribution measurement. Since,  $E1$  transitions are generally less mixed than  $M1$  or  $E2$ 's the 101 keV transition is ideally suited for the gating purpose for extracting the DCO ratios. The DCO ratios obtained by gating on the 101 keV transition which are close to  $\sim 1$  and  $\sim 2$  are assigned as  $\Delta J = 1$  and  $\Delta J = 2$  transitions, respectively.

Polarization asymmetry data as discussed earlier are used to extract the polarization of various states.

#### IV. COMPARISON WITH SHELL MODEL CALCULATIONS

The level structure of  $^{88}\text{Zr}$  developed in the present work has a similarity to that of  $^{90}\text{Mo}$  [29] suggesting the role of two neutron holes in various configurations. The level structure of  $^{88}\text{Zr}$  shows the characteristics of single-particle excitations.

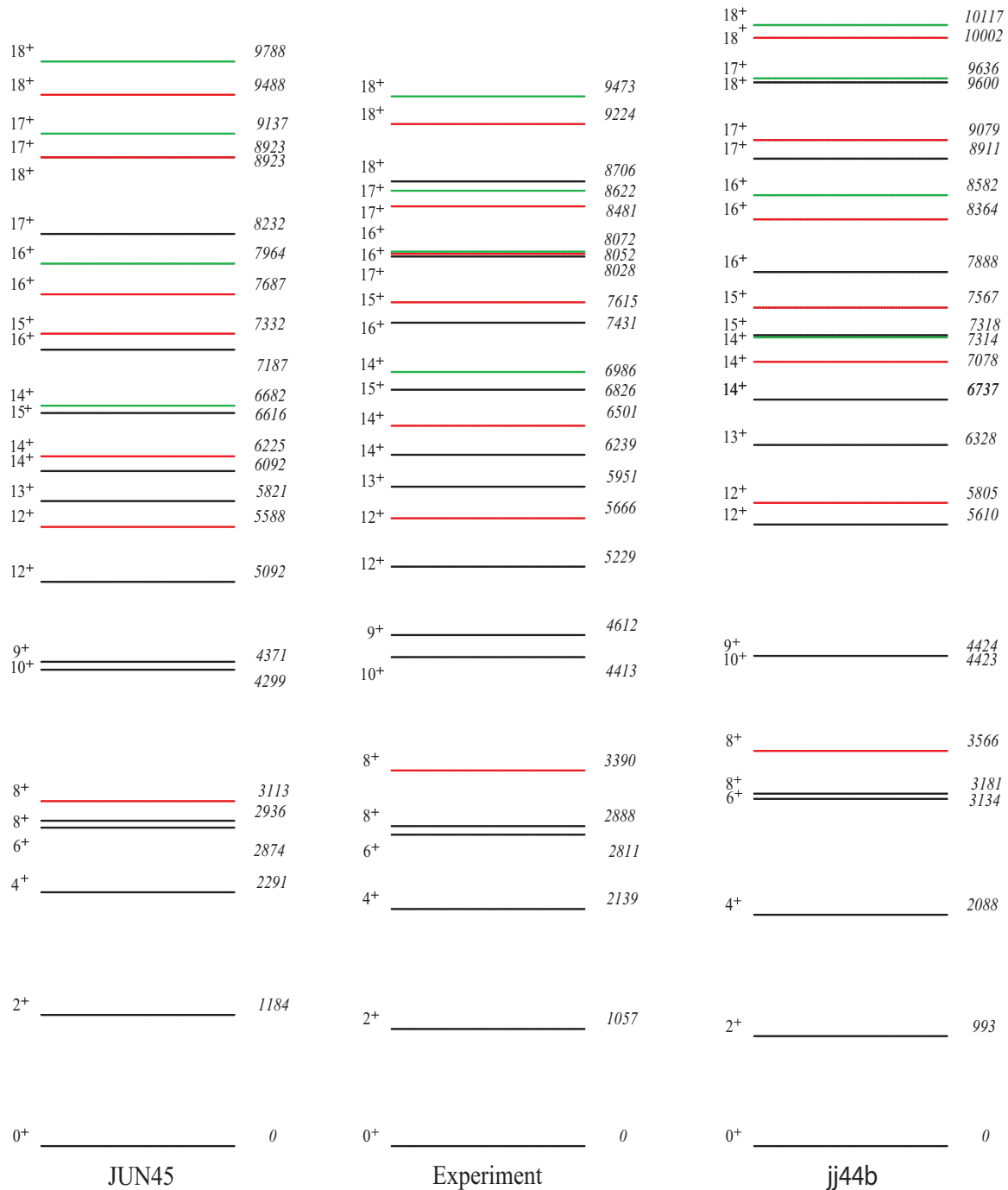


FIG. 7. (Color online) A comparison of the measured positive parity states (middle) of  $^{88}\text{Zr}$  with the shell model calculation using the JUN45 (left) and jj44b (right) interactions in the model space incorporating the  $p_{3/2}$ ,  $f_{5/2}$ ,  $p_{1/2}$ , and  $g_{9/2}$  orbitals. For a given spin whenever more than one state is present, they have been marked with red (second excited state) and green (third excited state).

State-of-the-art shell model calculations have been performed using two different interactions to interpret the experimental data of  $^{88}\text{Zr}$  up to the highest observed spin value. Previous shell model calculations reported for this nucleus were mostly carried out using the  $^{88}\text{Sr}$  core having only  $p_{1/2}$  and  $g_{9/2}$  orbitals available for excitation with two neutron holes and two proton particles [30–33]. The effect of particle excitation

from  $p_{3/2}$  and  $f_{5/2}$  orbitals was ignored [16]. However, it was noticed that the calculated energies as suggested by Gross and Frenkel [30] significantly deviate from the experimental level energies at low spin. This discrepancy was suggested due to the admixture of a quadrupole vibration in the  $0^+$ ,  $2^+$ , and  $4^+$  states and a modification to some of the matrix elements were proposed [16]. In our present work, two recent

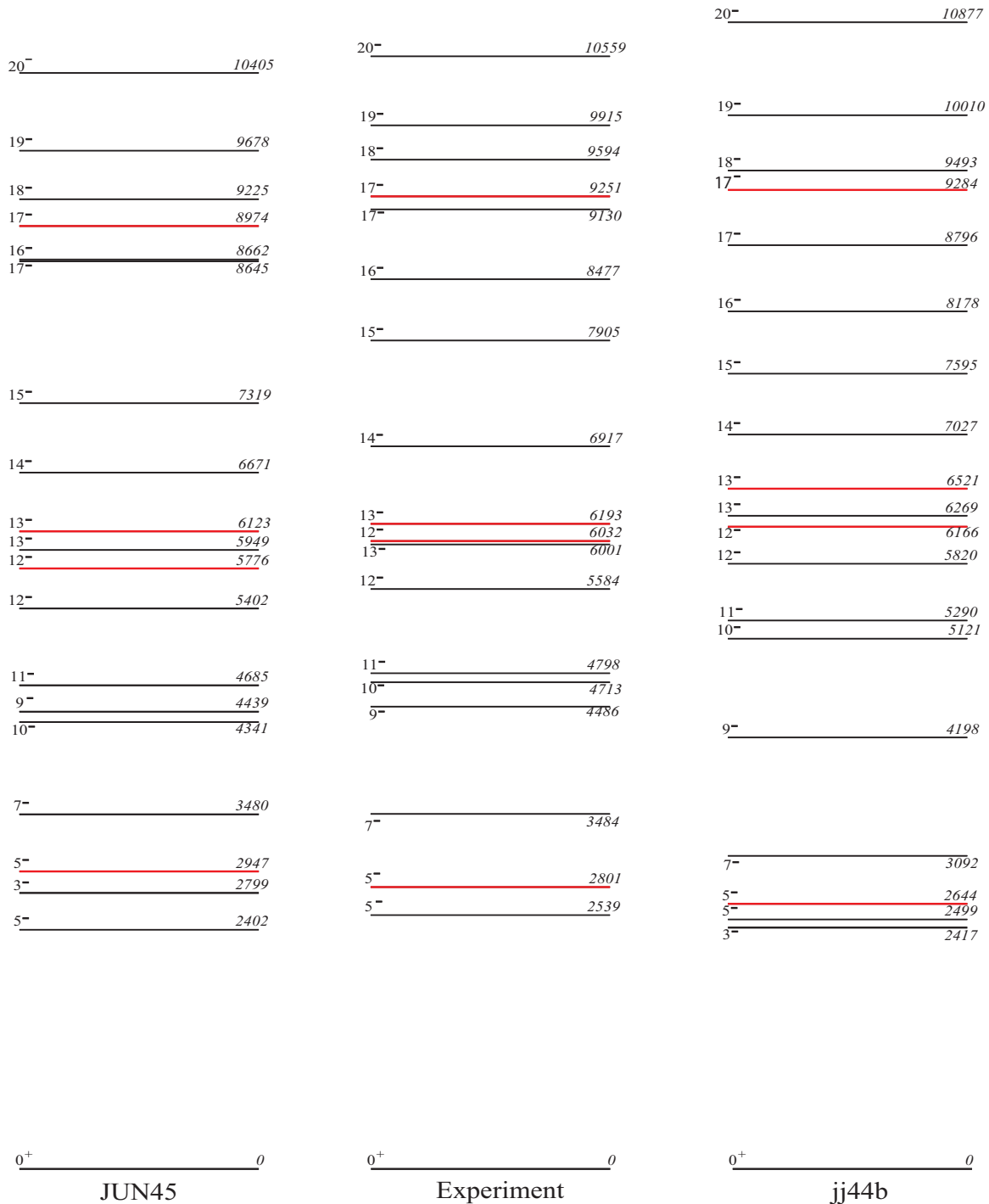


FIG. 8. (Color online) A comparison of the measured negative parity states (middle) of  $^{88}\text{Zr}$  with the shell model calculation using the JUN45 (left) and jj44b (right) interactions in the model space incorporating the  $p_{3/2}$ ,  $f_{5/2}$ ,  $p_{1/2}$ , and  $g_{9/2}$  orbitals. The second excited states observed for certain spin values have been marked as red.

interactions viz. JUN45 [5] and jj44b [7] have been used in the same form in which they have been optimized for the 28-50 valence shell without any modification. The calculations were performed using the shell-model code ANTOINE [34]. In the case of the jj44b interaction the single-particle energies are  $-9.6566$ ,  $-9.2859$ ,  $-8.2695$ , and  $-5.8944$  MeV and for the JUN45 interaction they are  $-9.8280$ ,  $-8.7087$ ,  $-7.8388$ , and  $-6.2617$  MeV for the  $p_{3/2}$ ,  $f_{5/2}$ ,  $p_{1/2}$ , and  $g_{9/2}$  orbits, respectively. The present calculation reproduces the experimental values well up to the highest observed spin. In Figs. 7 and 8 the comparison of the experimental excitation energies of the positive and negative parity states of  $^{88}\text{Zr}$  with the predictions of shell-model calculations obtained from the two different sets of effective interactions are shown. The calculated energy levels of both positive and negative parity states have been normalized with the  $J^\pi = 0_1^+$  ground state of  $^{88}\text{Zr}$ . The ground state wave function as predicted by both the interactions has the largest contribution from the  $\pi(p_{3/2}^4 f_{5/2}^6 p_{1/2}^0 g_{9/2}^2) \otimes \nu(p_{3/2}^4 f_{5/2}^6 p_{1/2}^2 g_{9/2}^8)$  configuration. However, a significant admixture from the  $\pi(p_{3/2}^4 f_{5/2}^6 p_{1/2}^2 g_{9/2}^0) \otimes \nu(p_{3/2}^4 f_{5/2}^6 p_{1/2}^2 g_{9/2}^8)$  configuration is also being predicted in the ground state. In all positive parity states starting from the ground state up to spin  $16^+$  a significant contribution has been observed from the  $\pi(p_{3/2}^4 f_{5/2}^6 p_{1/2}^0 g_{9/2}^2) \otimes \nu(p_{3/2}^4 f_{5/2}^6 p_{1/2}^2 g_{9/2}^8)$  configuration. Incidentally, the maximum spin that can be generated from this configuration is also  $16^+$ . Results from both the interactions

are found to be in reasonable agreement with the experimentally observed levels up to 9.5 MeV excitation energy. The calculation involving the JUN45 interaction shows overall better agreement for the positive parity states compared to the results based on jj44b interaction, particularly at higher spins. The difference between the positive parity experimental and calculated levels using the JUN45 interaction remains below 400 keV up to the highest spin. However, in case of the jj44b interaction, the deviation between calculated energy levels and measured levels has been observed to be as high as 1 MeV. The measured  $J^\pi = 10^+$  yrast state at 4413 keV is found to be 199 keV more bound compared to the  $J^\pi = 9^+$  yrast state. This observed feature of the ordering of  $J^\pi = 9^+$  and  $J^\pi = 10^+$  states has been qualitatively reproduced in the calculations with both the interactions. Certain discrepancies in the ordering of the positive parity states have been observed between measured levels and calculations beyond the  $J^\pi = 17^+$  state. The lowest negative parity state as predicted by the JUN45 interaction is  $5_1^-$  while the same for the jj44b interaction is  $3_1^-$  (see Fig. 8). However, in the present experiment no  $3^-$  state is observed. The experimentally observed  $5_1^-$  state with energy 2539 keV is reproduced in the calculations with a difference of less than 40 keV in the jj44b and 137 keV in the JUN45 interactions, respectively. Up to  $J^\pi = 11^-$ , the ordering of measured negative parity levels with increasing spin are exactly reproduced in the jj44b based calculation.

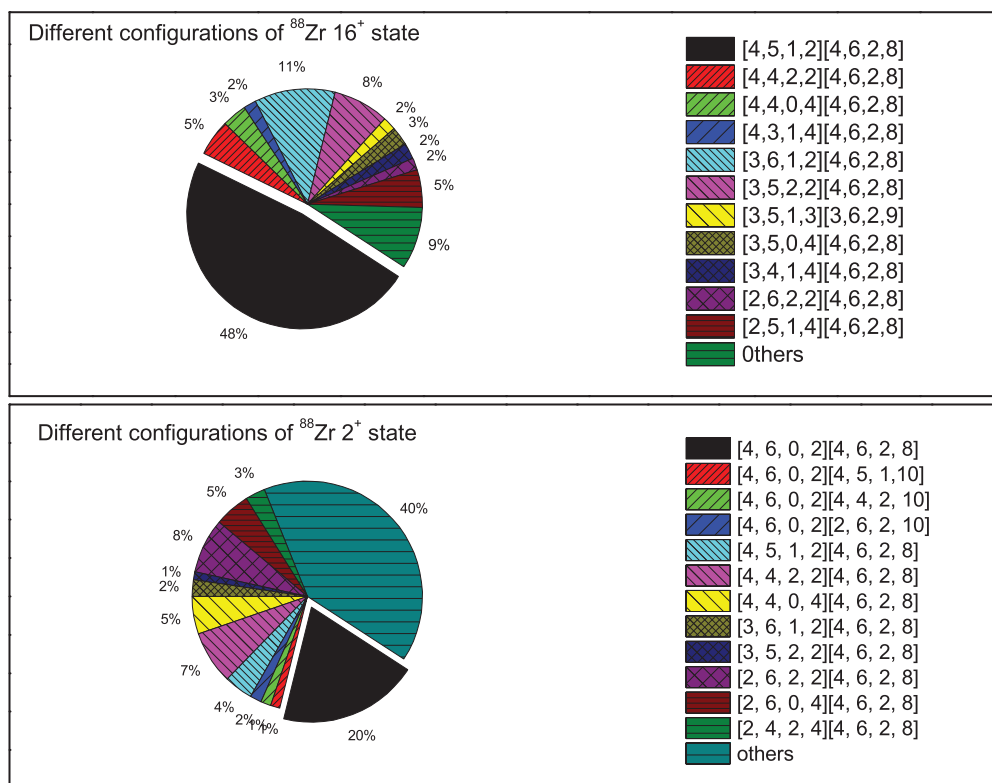


FIG. 9. (Color online) Contribution of different configurations in the yrast  $16^+$  and  $2^+$  levels as calculated with the JUN45 interaction are shown in the pie charts. The configuration which has the largest contribution is shown with black color. The figure shows larger configuration mixing in the  $2^+$  state than in the  $16^+$  state. The first and the second square brackets in the legend represent the number of protons and neutrons in different orbitals corresponding to various configurations, respectively. The entries in the square brackets corresponds to the number of particles in  $p_{3/2}$ ,  $f_{5/2}$ ,  $p_{1/2}$ , and  $g_{9/2}$ , respectively.

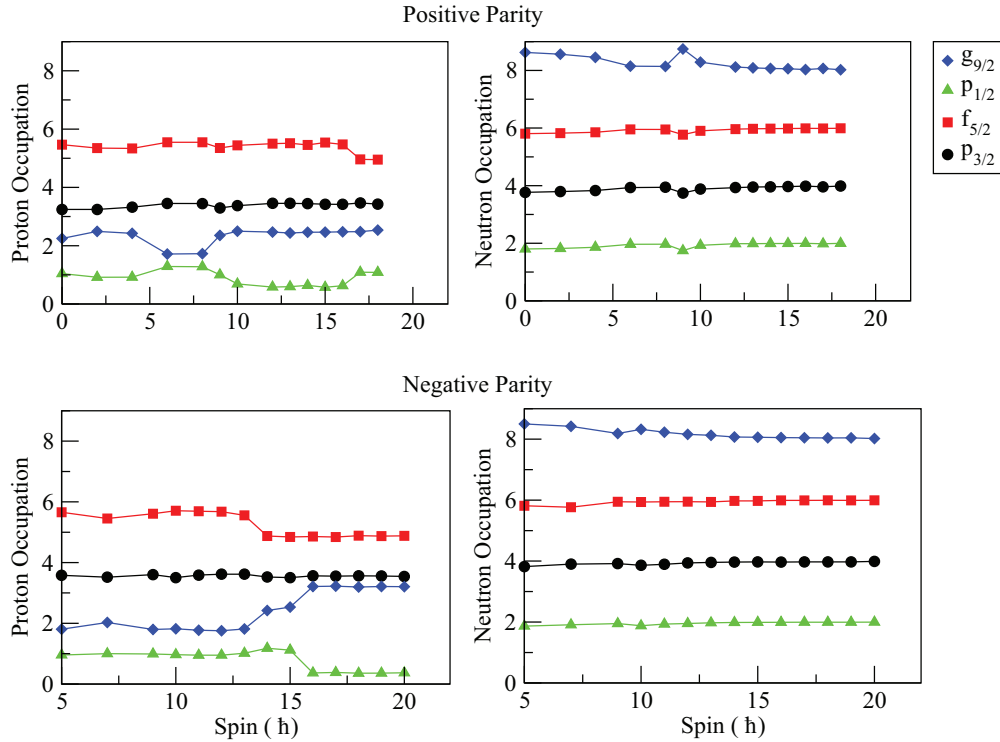


FIG. 10. (Color online) Shell model calculation of particle occupation with the JUN45 interaction for the observed yrast levels of  $^{88}\text{Zr}$  positive parity states showing the probability of protons occupying the  $g_{9/2}$  level is increased, whereas the same is decreased for the  $p_{1/2}$  and  $f_{5/2}$  levels at higher spin states. No significant change in particle occupation in  $p_{3/2}$  has been observed. In the neutron shell no significant change in particle occupation is observed.

However, the  $9_1^- - 10_1^-$  states have been predicted in reverse order for the case of the JUN45 interaction compared to the measured level scheme of  $^{88}\text{Zr}$ . A similar discrepancy of the JUN45 results with the experiment has also been observed for the ordering of the  $16_1^-$  and  $17_1^-$  states. Therefore, jj44b provides a comparatively better description of the negative parity states up to medium spin. For the three highest observed spin states with negative parity, both the interactions reproduce the excitation energy within 350 keV. From  $5^-$  up to  $13^-$  the negative parity states are primarily composed of the  $\pi(p_{3/2}^4 f_{5/2}^6 p_{1/2}^8 g_{9/2}^1) \otimes \nu(p_{3/2}^4 f_{5/2}^6 p_{1/2}^2 g_{9/2}^8)$  configuration. The calculated wave functions have a significant admixture of configurations involving excitation from  $f_{5/2}$  and  $p_{3/2}$  orbitals at low spins. The observed overall agreement of the experiment with the present shell model calculation in  $^{88}\text{Zr}$  up to the highest observed spin indicates the necessity of incorporating the full unrestricted  $f_{5/2} p g_{9/2}$  model space for the calculation in this mass region. The possible reason of the overestimation of energies in all the previous calculations is probably due to nonincorporating the large contribution from configurations involving excitation from  $f_{5/2}$  and  $p_{3/2}$  orbitals. However, relatively less configuration mixing was observed at higher spins. Experimentally, from spin  $14^+$  up to  $18^+$  all the levels in the positive parity have second or third excited states which is indicative of the fact that states of different configurations are less separated in energy due to reduced mixing. Relatively strong configuration mixing is observed for the low spin states in comparison to the high spin states. Again, the jj44b

interaction predicts more configuration mixing than the JUN45 interaction in most of the states. In Fig. 9 two pie charts are drawn from the results of the shell model calculation using the JUN45 interaction showing a contribution of different configurations in the yrast  $2^+$  and  $16^+$  states, respectively. In Fig. 10 the average occupation of protons and neutrons in different orbitals has been plotted with respect to the spin of the nucleus. The particle occupation in the  $g_{9/2}$  orbital for a proton is increased with spin. While, the same is reduced for  $f_{5/2}$  and  $p_{1/2}$  orbitals. This shows the excitation of a proton from  $f_{5/2}$  and  $p_{1/2}$  to the  $g_{9/2}$  orbital at higher spin. No significant change in proton occupation in the  $p_{3/2}$  orbital has been observed up to the highest spin. The excitation energy of the first  $2^+$ ,  $4^+$ ,  $6^+$ , and  $8^+$  level of  $^{88}\text{Zr}$  is smaller compared to that of  $^{90}\text{Zr}$ , which indicates that due to significant mixing of the  $\pi g_{9/2}^0 \nu g_{9/2}^{-2}$  configuration with the  $\pi g_{9/2}^2 \nu g_{9/2}^{-2}$  configuration, these states in  $^{88}\text{Zr}$  are suppressed in energies. Whereas, for  $^{90}\text{Zr}$  these states are more likely to be of two proton excitation only, as the  $N = 50$  shell closure prevents neutron excitation at low spin.

## V. CONCLUSION

High spin states of  $^{88}\text{Zr}$  were studied using the prompt as well as delayed coincidence technique. The level scheme has been considerably extended in the positive parity part. A rearrangement of levels has been made in the negative parity part of the level scheme. Angular correlation and polarization measurements were performed to assign the spin and parity

of the new levels and confirm that of the known levels. The persistence of single-particle type excitations in  $^{88}\text{Zr}$  up to  $J \leq 20$  indicates the dominance of its spherical shape in the entire range of measured spin and, thereby, providing a good testing ground for the residual interactions of shell model calculations. Large scale shell model calculations carried out to interpret the data have well reproduced the experimental level scheme up to the highest observed spin. The consistency in the results of the shell model calculation involving two interactions with full unrestricted  $f_{5/2}pg_{9/2}$  model space in both  $^{89}\text{Zr}$  [6] and  $^{88}\text{Zr}$  without any local adjustment in the level energies or interaction parameter shows the success of the microscopic calculation and the necessity of incorporating the full unrestricted model space for a calculation in this mass region. In particular, the role of proton excitation from the  $p_{1/2}$  and  $f_{5/2}$  to the  $g_{9/2}$  orbital is found to be crucial for the shell model calculations. The observed small discrepancies of the results of the JUN45

and jj44b interactions with the measured level scheme have also been discussed. The low spin states up to  $J^\pi = 8^+$  have been found to have a considerable mixing of configurations compared to the high spin states. On the experimental side, lifetime measurements will be useful to probe the configuration mixing in  $^{88}\text{Zr}$ .

#### ACKNOWLEDGMENTS

We gratefully acknowledge the INGA collaboration for making the detectors available and all the staff of the Pelletron Linac facility at TIFR, Mumbai for the smooth functioning of the accelerator. The help of B. S. Naidu, R. Donthi, S. Jadhav, and P. B. Chavan for the experimental setup is acknowledged. This work was partially funded by the Department of Science and Technology, Government of India (No. IR/S2/PF-03/2003-II).

- 
- [1] G. A. Jones *et al.*, *Phys. Rev. C* **76**, 054317 (2007).  
 [2] T. Fukuchi *et al.*, *Eur. Phys. J. A* **24**, 249 (2005).  
 [3] M. Bunce *et al.*, *Phys. Rev. C* **87**, 044337 (2013).  
 [4] N. Fotiadis *et al.*, *Phys. Rev. C* **74**, 034308 (2006).  
 [5] M. Honma, T. Otsuka, T. Mizusaki, and M. Hjorth-Jensen, *Phys. Rev. C* **80**, 064323 (2009).  
 [6] S. Saha *et al.*, *Phys. Rev. C* **86**, 034315 (2012).  
 [7] B. A. Brown and A. F. Lisetskiy (unpublished); see also endnote (28) in B. Cheal *et al.*, *Phys. Rev. Lett.* **104**, 252502 (2010).  
 [8] J. Flegenheimer, *Radiochim. Acta.* **6**, 20 (1966).  
 [9] T. A. Doron and M. Blann, *Nucl. Phys. A* **161**, 12 (1971).  
 [10] E. Bayar *et al.*, *Izv. Akad. Nauk. SSSR Ser. Fiz.* **38**, 666 (1974).  
 [11] K. Oxorn and S. K. Mark, *Z. Phys. A* **316**, 97 (1984).  
 [12] J. B. Ball *et al.*, *Phys. Rev.* **177**, 1699 (1969).  
 [13] J. B. Ball *et al.*, *Phys. Rev. C* **4**, 196 (1971).  
 [14] T. Numao, H. Nakayama, T. Kobayashi, T. Shibata, and Y. Kuno, *J. Phys. Soc. Jpn.* **46**, 361 (1979).  
 [15] J. E. Kitching, P. A. Batay-Csorba, C. A. Fields, R. A. Ristinen, and B. L. Smith, *Nucl. Phys. A* **302**, 159 (1978).  
 [16] K. Oxorn, S. K. Mark, J. E. Kitching, and S. S. M. Wong, *Z. Phys. A* **321**, 485 (1985).  
 [17] E. K. Warburton, J. W. Olness, C. J. Lister, R. W. Zurmuhle, and J. A. Becker, *Phys. Rev. C* **31**, 1184 (1985).  
 [18] R. Palit, in *Application of Accelerators in Research and Industry: Twenty-First International Conference*, edited by F. D. McDaniel and B. L. Doyle, AIP Conf. Proc. No. 1336 (AIP, New York, 2011), p. 573.  
 [19] R. Palit *et al.*, *Nucl. Instrum. Methods Phys. Res. A* **680**, 90 (2012).  
 [20] H. Tan *et al.*, *2008 IEEE Nuclear Science Symposium and Medical Imaging Conference (2008 NSS/MIC)*, Dresden, 2008 (IEEE, New York, 2009), p. 2471.  
 [21] D. C. Radford, *Nucl. Instrum. Methods Phys. Res. A* **361**, 297 (1995).  
 [22] A. Krämer-Flecken, T. Morek, R. M. Lieder, W. Gast, G. Hebbinghaus, H. M. Jäger, and W. Urban, *Nucl. Instrum. Methods Phys. Res. A* **275**, 333 (1989).  
 [23] K. S. Krane, R. M. Steffen, and R. M. Wheeler, *Nucl. Data Tables* **11**, 351 (1973).  
 [24] P. M. Jones *et al.*, *Nucl. Instrum. Methods Phys. Res. A* **362**, 556 (1995).  
 [25] Lawrence W. Fagg and Stanley S. Hanna, *Rev. Mod. Phys.* **31**, 711 (1959).  
 [26] K. Starosta *et al.*, *Nucl. Instrum. Methods Phys. Res. A* **423**, 16 (1999).  
 [27] R. Palit, H. C. Jain, P. K. Joshi, S. Nagaraj, B. V. T. Rao, S. N. Chintalapudi, and S. S. Ghugre, *Pramana* **54**, 347 (2000).  
 [28] Y. Zheng *et al.*, *Phys. Rev. C* **87**, 044328 (2013).  
 [29] S. E. Arnell *et al.*, *Phys. Scr.* **46**, 389 (1992).  
 [30] R. Gross and A. Frenkel, *Nucl. Phys. A* **267**, 85 (1976).  
 [31] I. Talmi and I. Unna, *Nucl. Phys.* **19**, 225 (1960).  
 [32] F. J. D. Serduke, R. D. Lawson, and D. H. Gloeckner, *Nucl. Phys. A* **256**, 45 (1976).  
 [33] H. Herndl and B. A. Brown, *Nucl. Phys. A* **627**, 35 (1997).  
 [34] E. Caurier, G. Martínez-Pinedo, F. Nowacki, A. Poves, and A. P. Zuker, *Rev. Mod. Phys.* **77**, 427 (2005).